A new actin depolymerase: a catch bond Myosin 1 motor

Julien Pernier[1,2,3]+, Remy Kusters[1,2,4]+, Hugo Bousquet[2,3], Thibaut Lagny[1,2,3], Antoine Morchain[1,2], Jean-François Joanny[1,2,5,6*], Patricia Bassereau[1,2]*, Evelyne Coudrier[2,3]*

1. Laboratoire Physico-Chimie Curie, Institut Curie, PSL Research University, CNRS UMR168, 75005 Paris, France
2. Sorbonne Université, 75005 Paris, France
3. Institut Curie, PSL Research University and C.N.R.S. UMR 144, 26 rue d'Ulm, Paris, France
4. University Paris Descartes, Center for Research and Interdisciplinarity (CRI), 8 Rue Charles V, Paris, France
5. ESPCI Paris, PSL Research University, 10 rue Vauquelin 75005 Paris, France
6. Collège de France, 11 Place Marcelin Berthelot, 75231 Paris Cedex05, France

+ : equally contributing authors
*: corresponding authors: jean-françois-joanny@curie.fr, patricia.bassereau@curie.fr and evelyne.coudrier@curie.fr

Abstract

The regulation of actin dynamics is essential for various cellular processes. Former evidence suggests a correlation between the function of non-conventional myosin motors and actin dynamics. We investigate the contribution of the catch-bond myosin1b to actin dynamics using sliding motility assays. We observe that sliding on myosin1b immobilized or bound to a fluid bilayer enhances actin depolymerization at the barbed end, while sliding on the weak catch-bond myosin II has no effect. Our theoretical model shows the pivotal impact of the catch-bond behavior of a motor on depolymerization of sliding actin filaments. The catch-bond prolongs the attachment time of the motor at the barbed end due to the friction force exerted by the sliding filament; thereby this motor exerts a sufficient force on this end to promote depolymerization. This work reveals a non-conventional myosin motor as a new type of depolymerase.

1 Actin filaments (F-actin) form a variety of dynamical architectures that govern cell
2 morphology and cell movements. The dynamics of the actin networks are regulated in space
3 and time by the assembly and disassembly of actin polymers under the control of regulatory
4 proteins. Cortical actin organizes lateral movement of transmembrane proteins and
5 participates in membrane signaling by interacting transiently with the plasma membrane [1].
6 One class of actin-associated molecular motors, the single-headed myosin 1 proteins, bridges
7 cortical actin to the plasma membrane. Polymerization of actin filaments at the plasma
8 membrane generates forces on the membrane as well as on their membrane linkers. Inversely
9 myosin 1 can exert and sustain pN forces on F-actin [2].
10 This important class of myosins contains a motor domain at its N-terminus that binds F-
11 actin in response to ATP hydrolysis, a light chain binding domain (LCBD) that binds
12 calmodulin (in most cases), and a Tail domain at the C-terminus (Fig. 1A) [3]. The Tail domain
13 encompasses a tail homology domain (TH1) with a pleckstrin homology motif (PH) that binds
14 phosphoinositides (Fig. 1A). Beside the involvement of myosin 1 proteins in a large variety of
15 cellular processes including cell migration and membrane trafficking [3], manipulation of
16 myosin 1 expression has revealed a correlation between these myosins and actin network
17 architecture [4, 5, 6, 7]. In particular, under- or overexpression of one of these myosins, myosin 1b
18 (Myo1b), affects the organization of the actin cytoskeleton in the juxtanuclear region of HeLa
19 cells [4] and in growth cones of cortical neurons [6]. However, the role of these motors in actin
20 dynamics remains to be explored.
21 When bound to a substrate and in contact with F-actin, Myo1b has different
22 configurations over time as a function of the ATP hydrolysis stage. When attached, Myo1b
23 performs a first power-stroke and propels the actin filament over a distance d_1 towards the
24 minus-end (being a plus-end motor) and depending on the applied force, it performs a second
25 power stroke over a distance d_2. Myo1b being a catch bound motor (the time Myo1b remains
26 bound to F-actin strongly increases with an applied load), it thus remains attached to the
27 filament for a time that depends on the applied force F. It eventually detaches independently
28 of the force but depending on the ATP concentration with a rate $\varpi_{det}(C_{ATP})$ [9] (Fig. 1B). Due
29 to its mechanosensitive behavior, Myo1b could in turn exert a force on actin filaments [8, 9] and
30 thus affect their polymerization. In this paper, we use *in vitro* F-actin gliding assays (Fig. 1C)
31 and total internal reflection fluorescence (TIRF) microscopy to study the effect of Myo1b on
32 actin polymerization dynamics, with the motors either immobilized on a solid substrate (Fig.
33 1C, III) or bound to a fluid supported bilayer, which mimics cell membranes (Fig. 1C, IV).
34 The sliding velocity v_f of single stabilized F-actin on Myo1b immobilized on a glass
35 coverslip (Fig. S1A, top and Movie S1), the sliding velocity v_f and the polymerization rate v_p
36 (expressed in actin sub-unit/s, with the length of an actin subunit being equal to 2.7 nm) of
37 single F-actin (Fig. S1A, bottom and Movie S1) (Materials and Methods), both in the
38 presence of 0.3% methylcellulose for keeping the filaments in the TIRF field, were measured
39 by image analysis. At high Myo1b density (8000 μm^{-2}) (for the motor density measurement,
40 see Materials and Methods and Fig. S1B), both stabilized and polymerizing filaments move
41 with the same average sliding velocity $v_f = 56.4 \pm 15.4$ nm.s^{-1} and $v_f = 53.9 \pm 5.5$ nm.s^{-1},
42 respectively (Fig. 2A, Fig.2B, Movie S1 and Table S1) in the presence of 2 mM ATP (above
43 saturation for motor activity) [10]. In both cases, this velocity decreases by about a factor two
44 when decreasing the Myo1b density by a factor of twenty (Fig. S2B, S2C, Table S1) or when
45 reducing the ATP level to 0.2 mM (Fig. 2A,B, Movies S2, S3) below saturation for Myo1b,
46 but not affecting actin polymerization (Table S2).
47 To describe the actin filament sliding on Myo1b taking into account the force and ATP
48 dependence, we extend the two state cross-bridge model [11] to a three-state cross-bridge model
49 in order to explicitly include the two distinct sub-steps observed by Laksoo et al. [9]; (Fig. 1B,
50 Material and Methods). Increasing the ATP concentration increases the filament sliding

51 velocity v_f, while the fraction of motors in the ATP-dependent sub-step 2 decreases; however
52 it lowers the catch-bond dependent transition rate, $\omega_{1\text{-}2}$ (Fig. 1B). This in turn increases the
53 time that the catch-bond motor spends in the ADP state, as compared to what happens for a
54 weakly catch-bond motor such as myosin II (Fig. S3E). By matching the force-dependent
55 transition rate ($\omega_{1\text{-}2}$) and the ATP dependent detachment rate (ω_{det}) we calculate the stationary
56 sliding velocity of the filament, at the two measured ATP concentrations ($v_f \approx 55\,nm/s$ at
57 $C_{ATP} = 2mM$ and $v_f \approx 25\,nm/s$ at $C_{ATP} = 0.2mM$, Fig. S3F) for Myo1b as well as for
58 MyoII ($v_f \approx 255\,nm/s$ at $C_{ATP} = 2mM$). This model describes accurately the effect of the
59 catch-bond on the sliding velocity (Fig. S3F).
60   We next investigated the impact of Myo1b on actin polymerization upon filament
61 sliding. The actin assembly-disassembly kinetics are an order of magnitude faster at the
62 barbed (plus) end than at the pointed (minus) end [12]. Thus, we measured the elongation ΔL of
63 F-actin at the barbed-end versus time (Fig. 2C). Strikingly, filament sliding on Myo1b
64 decreases the actin polymerization rate v_p, as compared to actin polymerization in the absence
65 of Myo1b (Fig. 2D and Movie S3). This effect is stronger for high filament sliding velocity
66 (in the presence of 2 mM ATP) and weaker at lower Myo1b density on the substrate (Figs.
67 S2B, S2D, Movie S3 and Table S2). We also measured the dynamics of the pointed (minus)
68 end by detecting the relative movement of this extremity compared to a fiducial point on the
69 filament. In contrast with the barbed end, we did not observe any filament length variation
70 (Fig. S2A and Movie S4), thus filament sliding on the motors reduces the actin
71 polymerization rate at the barbed-end only. As a control, we tested the impact on actin
72 polymerization of free Myo1b present only in the bulk, or immobilized on the surface but
73 inactivated (Figs. S2B,D and Movie S5); we did not observe any effect on polymerization
74 (Fig. S2E). Moreover, although actin filaments slide five-fold faster on non- or weak catch-
75 bond myosins such as muscle myosin II (MyoII) [13], at the same bulk monomeric-actin (G-
76 actin) concentration (Fig. 2A,B and Movie S6), the actin polymerization rate remains similar
77 to the control (Fig. 2C, D). These observations demonstrate that an immobilized myosin
78 motor with intact activity and a catch-bond behavior reduces the actin polymerization rate at
79 the barbed-end up to a factor two (Fig. 2D and Table S2), in contrast to a weak catch-bound
80 myosin such as muscle MyoII.
81   Dynamics at the barbed-end results from a balance between the rate of association of G-
82 actin k_{on} and the rate of dissociation k_{off}; steady state is obtained at the critical concentration
83 C_{c^+}. Classically, these dynamical parameters are deduced from the measurement of the
84 variation of the polymerization rate v_p with G-actin concentration C_m: $v_p = k_{on}C_m - k_{off}$.
85 By varying the G-actin bulk concentration from 0.1 to 1 µM in the presence of either 0.2 mM
86 and 2 mM ATP, we observed that the slope corresponding to k_{on} is unchanged when F-actin
87 slides over Myo1b, whereas C_{c^+} which is the ratio between k_{off} and k_{on} increases (Fig. 2D)
88 demonstrating that k_{off} increases under these conditions (Fig. 2D and Table S2). Still, in the
89 absence of G-actin in the bulk, filaments depolymerize faster when they slide over Myo1b
90 (Fig. S2F, G and Movie S7). Interestingly, the dissociation rate is weakly affected when
91 reducing Myo1b density (Fig. S2E and Table S2). The decrease of the dissociation rate is due
92 to a lower sliding velocity of the filament. As expected, the sliding velocity of the filament
93 decreases weakly with the motor density. In our model, this effect is associated with the
94 impact of the external hydrodynamic drag on the filament, which eventually slows down the
95 motors. In contrast, while sliding on MyoII is much faster, this myosin has no influence on
96 k_{off} at the barbed-end of the filament (Fig. 2D and Table S2). Together, these observations
97 indicate that the catch-bond Myo1b is an actin depolymerase.
98   One possible mechanism for this depolymerase activity is that Myo1b induces actin
99 depolymerization by modulating the torsion of the filaments [14]. In this case, the

4

100 polymerization kinetics is expected to depend on the filament length with a twist gradient
101 inversely proportional to the length. However this is not what we observe (Fig. S2H),
102 excluding an explicit role of filament torsion due to motor attachment along the filament.
103   We thus developed a theoretical model for actin polymerization when filaments slide on
104 motors depending on their catch-bond properties (Fig. 1B, Fig. 2E, and Materials and
105 Methods). Due to the catch-bond behavior of Myo1b, the transition rate between sub-step 1
106 and sub-step 2 in Fig. 1B decreases with increasing filament sliding velocity. Thus, the
107 motors remain in the ADP state for an increased time, inducing a larger friction on the sliding
108 filaments as compared to non-catch-bond motors such as MyoII. We assume that this friction
109 between the motor and the filament increases the attachment time of the single molecular
110 motor at the barbed end and thus this motor induces a force F_{mot} at this extremity sufficient to
111 promote depolymerization (Fig. 2E). We have quantified this effect by assessing the impact of
112 the friction force on the increase of the actin dissociation rate. For this we have introduced an
113 exponential decay of the dissociation rate with the force on the filament over a characteristic
114 force $f*$ [15] (Materials and Methods Eq. SE10). This characteristic force quantifies the force
115 sensitivity of the depolymerization rate of actin k_{off}. Using our model we have determined
116 $3.5 pN < f < 4.5 pN$ (Fig. S5A). $f \gg 5 pN$ would make the actin filament insensitive to
117 forces applied by the motor (Fig. S5A). $f \ll 3 pN$ would impact the dissociation at low ATP
118 concentration, precluding the stability of the filaments in the presence of motors (Fig. S5A).
119 This model shows that the catch-bond behavior of Myo1b strongly increases the F-actin
120 depolymerization at the barbed-end while a weakly-catch bond MyoII motor barely impacted
121 F-actin depolymerization in agreement with our experiments.
122   In cells, Myo1b is bound to the fluid plasma membrane lipid bilayer through the
123 interaction of its PH domain with PI(4,5)P2 [16], and thus it is not immobilized (Fig. 3A). We
124 mimic experimentally these cellular conditions by analyzing the impact of Myo1b on actin
125 dynamics when bound to a glass-supported lipid bilayer (SLB) composed of 79.5% POPC,
126 20% L-α-phosphatidylinositol-4,5-bisphosphate (PI(4,5)P2) and 0.5% Rhodamine-PE or
127 Atto488-DOPE (mol/mol) (Fig. 1C and Fig. 3) (Materials and Methods). We checked using
128 fluorescence recovery after photobleaching (FRAP) that membrane fluidity was preserved in
129 the SLB with bound Myo1b (Fig. 3A and Fig. S6). The lipid diffusion coefficient was in
130 agreement with data published on SLBs composed of pure POPC [17]. After recruitment on the
131 SLB, Myo1b diffuses freely in the plane of the membrane (Fig. 3A). We did not observe any
132 difference between experiments with or without methylcellulose in the bulk (Fig. 3A). In
133 addition, the lipids continue to diffuse freely even when Myo1b diffusion is strongly
134 decreased by a dense actin network (Fig. 3A) due to an emerging coupling when a filament
135 bridges multiples motors. The diffusion coefficients are close to those measured in cell
136 membranes (Fig. 3A), showing that in our *in vitro* experiments, the fluidity of the membrane
137 is preserved. As previously reported [18], myosin 1 proteins bound to a lipid bilayer exert a
138 force strong enough to propel actin filaments in spite of the fluidity of the support. We
139 confirmed that in the presence of 2 mM ATP and at a similar Myo1b density as when
140 immobilized (8500 µm^{-2}), stabilized and polymerizing F-actin slides on Myo1b bound to
141 SLBs, although with a velocity reduced by about 25%: $v_f = 37.6 \pm 7.3$nm.s^{-1} and $v_f = 39.3 \pm$
142 8.2nm.s^{-1} respectively (Fig. 3B, Fig. 3C, Movie S8 and Table S1).
143   We have calculated the relative contributions of the viscous drag of the bulk and of the
144 lipid bilayer on the motion of the filaments. First, we have considered F-actin moving in
145 water ($\eta_b = 10^{-3} Pa.s$) above Myo1b bound to a SLB (Fig. 3D). We estimate that, since the
146 in-plane viscous drag between the motor and the lipid bilayer is much larger than the bulk
147 viscosity experienced by the actin filaments, the velocity of the filament-motor couple, v_m,
148 practically vanishes. Thus, filaments slide with a velocity v_f similar to that measured for
149 immobilized motors: $v_f \approx v_f$ (Fig. S7). Including the increased viscosity of the bulk in the

150 presence of methylcellulose (10^{-2} Pa.s at 0.3%, product information Sigma) and crowding
151 effects between nearby filaments reduces the effective sliding speed of the filament v_f since
152 part of the sliding is dissipated by in-plane motion of the motors in the bilayer (Fig. S7). This
153 can explain why in our experiments, F-actin moves over SLB-bound Myo1b but with a
154 slightly reduced velocity as compared to immobilized Myo1b (Fig. 3C, Table S1). This is in
155 line with the results by Grover et al [19] showing a decreased gliding velocity of membrane-
156 anchored kinesins due to their slippage in the lipid bilayer.
157   In these experimental conditions, we observed a significant increase of the actin
158 depolymerization rate at the barbed end k_{off} when filaments slide on Myo1b bound to a SLB,
159 although weaker than for immobilized Myo1b, while keeping the polymerization rate
160 unchanged (Fig. 3E, Fig. 3F and Table S2). We conclude that the dissipation of sliding
161 filaments in SLBs is low enough to let Myo1b exert a significant dissociation force even
162 when bound to a fluid membrane (See force balance in Fig. 3G).
163   As previously shown, MyoII induces actin network contraction, potentially leading to
164 filament buckling and breaking [20, 21]. However, we show here that muscle MyoII which is a
165 weak catch-bond [13] in the pN force range, does not affect actin polymerization dynamics.
166 Different actin-binding proteins are already known for preventing actin polymerization
167 (capping protein) [12], enhancing it (formin) [22, 23] or depolymerizing actin (ADF/cofilin) [24, 25] at
168 the barbed end. Also, some kinesin motors, e.g., kinesins 8 and 13, have been shown to
169 depolymerize microtubules [26, 27]. We show here for the first time that increasing the sliding
170 speed of the actin filaments through increasing the ATP-concentration strongly impacts the
171 actin dissociation rate k_{off} at the barbed-end in a significant way only for catch-bond motors
172 (Tables S1 and S2). Note that the catch-bond effect on the actin growth is due to the longer
173 attachment time of the Myo1b motor, but other molecular mechanisms that increase the duty
174 ratio would potentially lead to a similar effect on actin dissociation. Another Myosin 1
175 (Myosin 1c) that is also a catch-bond, might regulate actin dynamics at the barbed-end.
176 Nevertheless, the lifetime of its attachment to actin under load is ten times lower than for
177 Myo1b [28], thus we expect its impact on actin dynamics to be moderate as compared to
178 Myo1b, but this remains to be tested.
179   Experimental evidence supports a role of several Myosin 1 proteins in membrane
180 remodeling [3]. Similarly to capping proteins [29], Myo1b and perhaps other Myosin 1 proteins
181 could shape membranes by regulating the growth of filaments at the plasma membrane.
182 Further experiments need to be performed in the future to determine the relative contribution
183 of Myo1b with respect to the other binding proteins. Alternatively, Myo1b could shape
184 membranes by inducing stresses in the cortical actin. Indeed, Myo1b induces actin movement
185 and reduces actin growth when bound to supported bilayers, as shown in our experiments.
186 Since the fluidity of our synthetic membranes and of cellular membranes are similar (Fig.
187 3A), we propose that Myo1b has the same function in cells. Collectively, these motors could
188 drive the sliding of actin filaments at the membrane surface, which could create stresses that
189 relax by deforming the cortex and the attached membrane. Interestingly, when Myo1b is
190 bound to a deformable giant liposome, we observed that it produces membrane invaginations
191 in presence of stabilized actin filaments (Fig. S8).
192   Myo1b's influence on actin dynamics can control the organization of actin networks, as
193 reported in growth cones [6]. An actin network can be impacted by Myo1b in different ways. It
194 can reduce the length of actin filaments, as shown by this work, and thus change the mesh-
195 size, or the cortical thickness and consequently the cortical contractibility [30]. Whether or not it
196 can affect the Arp2/3-dependent branched actin network and/or formin-dependent actin
197 bundles remains to be explored. Moreover, since Myo1b is specifically present at the interface
198 between the plasma membrane and the cortical actin, Myo1b may coordinate receptor
199 signaling by arranging the cytoskeleton [31].

200   Besides myosin II and myosin 1 proteins, myosin VI has also been reported to influence
201 the actin architecture during, e.g. spermatid individualization in Drosophila [32] or around
202 melanosomes [33]. It might be time now to take a fresh look on the involvement of non-
203 conventional myosins in actin dynamics and organization.
204

Materials and Methods

Protein purification

Actin was purified from rabbit muscle and isolated in monomeric form in G buffer (5 mM Tris-HCl, pH 7.8, 0.1 mM $CaCl_2$, 0.2 mM ATP, 1 mM DTT and 0.01% NaN_3). Actin was labeled with Alexa 594 succimidyl ester-NHS [34].

Myosin II was purified from rabbit muscle as previously described [35].

Expression and purification of Myosin 1b: FLAG-myo1b was expressed in HEK293-Flp-In cells cultured in Dulbecco's modified Eagle medium supplemented with 10% fetal bovine serum and 0.18 mg ml^{-1} hygromycine in a spinner flask at 37 °C under 5% CO_2, and collected by centrifugation (1,000 g, 10min, 4 °C) to obtain a 4–5 g of cell pellet. The pellet was lysed in FLAG Trap binding buffer (30 mM HEPES, pH 7.5, 100 mM KCl, 1 mM $MgCl_2$, 1mM EGTA, 1 mM ATP, 1 mM DTT, 0.1% protease inhibitor cocktail (PIC), 1% Triton X-100) for 30 min at 4 °C and centrifuged at 3,400 g for 10 min at 4 °C. The collected supernatant was then ultracentrifuged (250,000 g, 60 min, 4 °C). The solution between pellet and floating lipid layer was incubated with 150 µl of anti-FLAG beads for 2 h at 4 °C. The beads were collected by centrifugation (1,000 g, 5 min, 4 °C). After a washing step, FLAG-myo1b was then eluted by incubating with 0.24 mg ml^{-1} of 3X FLAG peptide in 300 µl elution buffer (binding buffer without Triton X-100 supplemented with 0.1% methylcellulose) for 3 h at 4 °C. After removal of the beads by centrifugation (1,000 g, 3 min, 4 °C), the protein solution was dialyzed against elution buffer overnight at 4 °C to remove the 3X FLAG peptide. Myo1b was fluorescently labeled using Alexa Fluor 488 5-SDP ester [36]. Inactivated Myo1b was removed by ultracentrifugation (90,000 rpm, 20 min, 4 °C) with 10 µM F-actin in presence of 2 mM ATP. Inactivated Myo1b was then dissociated from F-actin by incubating the pellet collected after untracentrifugation in elution buffer (30 mM HEPES, pH 7.5, 100 mM KCl, 1 mM $MgCl_2$, 1mM EGTA, 1 mM ATP, 1 mM DTT and 0.1% methylcellulose) supplemented with 1 M NaCl and collected in the supernatant after a second centrifugation (90,000 rpm, 20 min, 4 °C).

Supported lipid bilayer (SLB) preparation

SLBs were formed by fusion of small unilamellar vesicles (SUVs) prepared as follows. Lipid mixtures containing 79.5 % POPC, 20 % L-α-phosphatidylinositol-4,5-bisphosphate (PI(4,5)P_2) and 0.5 % Rhodamine-PE or Atto488-DOPE (mol/mol) were mixed together in a glass vial, dried with N_2, placed in vacuum desiccator for 1 hour, then rehydrated with Fluo F buffer (5 mM Tris-HCl- pH 7.8, 100 mM KCl, 1 mM $MgCl_2$, 0.2 mM EGTA, 0.2 mM or 2 mM ATP, 10 mM DTT, 1 mM DABCO, 0.01% NaN_3) for 30 min at room temperature, to a final lipid concentration of 2 mg/mL. After rehydration, the glass vial was vortexed to detach the liposomes. SUVs were formed by sonication, aliquoted and stored at -20 °C. For SLB formation by fusion, $CaCl_2$ was added to a final concentration of 5 mM, with 50 µl of SUVs. The solution was incubated in the chamber for 20 min and washed 5 times with Fluo F buffer 0.1 % BSA. The quality of the SLB was checked by FRAP.

Giant unilamellar vesicle (GUV) preparation

Lipid compositions for GUVs were 79.7 % POPC, 20 % L-α-phosphatidylinositol-4,5-bisphosphate (PI(4,5)P$_2$) and 0.3 % Texas Red DHPE. GUVs were prepared by using polyvinyl alcohol (PVA) gel-assisted method in a 200 mM sucrose buffer at room temperature for 2 hour as described previously [37].

Myosin 1b surface density

We measured the protein surface density (number of proteins per unit area) on solid surfaces or on SLBs by using a previously established procedure [38, 39]. It is calculated from a labeled proteins/lipids calibration. We first measure the fluorescence of POPC SLBs containing predefined amounts of Atto488-DOPE fluorescent lipids (DOPE*) to establish the relationship between the density of DOPE* n_{DOPE*} and the corresponding fluorescence intensity $I_{DOPE*\ SLB}$ (Fig. S1Ba). Assuming an area per POPC of 0.68 nm^2, we derive the calibration coefficient A corresponding to the slope of this curve. Note that A depends on the illumination and recording settings of the microscope.

$$n_{DOPE*} = A \times I_{DOPE*\ SLB}$$

Since Myo1b is labeled with Alexa488 and not Atto488, we have to correct this value by the ratio of fluorescence of the two fluorescent dyes in bulk deduced from the slope of the titration curves $\frac{I_{Alexa488}}{I_{DOPE}}$ (Fig. S1Bb and c). We then obtained the surface density of the protein deduced from the measurement of the Myo1b-Alexa488 intensity I_{Myo1b*} as:

$$n_{Myosin1B} = \frac{A}{\frac{I_{Alexa488}}{I_{DOPE}} \times Z} \times I_{Myo1b*}$$

where Z is the degree of labeling for the protein of interest (Here, $Z=1$). In our experiments, the calibration factor $\frac{A}{\frac{I_{Alexa488}}{I_{DOPE}} \times Z}$ is equal to 0.278.

Single-filament TIRF microscopy assays

The kinetics of single filament assembly was monitored by TIRF microscopy (Eclipse Ti inverted microscope, 100X TIRF objectives, Quantem 512SC camera). The experiments were controlled using the Metamorph software. Coverslips and glass slides were sequentially cleaned by sonication with H_2O, ethanol, acetone for 10 min, then 1M KOH for 20 min and H_2O for 10 min. In the case of supported lipid bilayer, first the coverslips and glass slides were cleaned by sonication with Hellmanex III (Hellma Analytics) for 30 min. Flow chambers were assembled with a coverslip bound to a glass slide with two parallel double-stick tapes. The chamber was incubated with 100 nM anti-myo1b antibody in G buffer (5 mM Tris-HCl, pH 7.8, 0.1 mM $CaCl_2$, 0.2 mM ATP, 1 mM DTT and 0.01% NaN_3) for 10 min at room temperature. The chamber was rinsed three times with buffer G 0.1 % BSA and incubated 5 min at room temperature. Then the chamber was incubated with 300 nM Alexa488-labeled myo1b in Fluo F buffer (5 mM Tris-HCl, pH 7.8, 100 mM KCl, 1 mM $MgCl_2$, 0.2 mM EGTA, 0.2 mM or 2 mM ATP, 10 mM DTT, 1 mM DABCO, 0.01% NaN_3) for 10 min at room temperature. Assays were performed in Fluo F buffer, containing 0.2 or 2 mM constant ATP, supplemented with 0.3% methylcellulose (Sigma) and with G-actin (10 % Alexa594) or F-actin (stabilized with phalloidin-Alexa594) at indicated concentrations. To maintaining a constant concentration of ATP in this assay an ATP regenerating mix, including 2 mM ATP, 2 mM $MgCl_2$, 10 mM creatine phosphate and 3.5 U/mL creatine phosphokinase, which constantly re-phosphorylates ADP into ATP to maintain a constant concentration of free ATP, was added.

The sliding and elongation velocities of actin filaments were analyzed by using Kymo Tool Box plugin of Image J software (https://github.com/fabricecordelieres/IJ_KymoToolBox). Only filaments longer than 20 pixels are analyzed. When filaments slide on myosins, only those moving directionally during the whole sequence are selected. On each image of a sequence, a segmented line is manually drawn over a single filament, which generates a 10 pixel wide band. The plugin flattens the curved filaments and generates a kymograph. The accuracy on the displacement and the length of the filaments is of the order of the pixel size (160 nm). We consider that each actin subunit contributes to 2.7 nm of the filament length.

FRAP methods

For diffusion measurements, Fluorescence Recovery After Photobleaching (FRAP) experiments were performed through a X100 or X60 oil immersion objective on an inverted spinning disk confocal microscope (Nikon eclipse Ti-E equipped with a Prime 95B™ Scientific CMOS camera, Photometrics) equipped with a FRAP unit. Recovery curves (average of 5 independent experiments, performed on different circular regions of the SLB using the same bleaching conditions) were normalized to the initial intensity and fitted with a single exponential function. We derive the $\tau_{1/2}$ time corresponding to the time at which the fluorescence signal has recovered 50% of its value before bleach. We calculated the diffusion coefficient using the Soumpasis equation[40]:

$$D_r = 0.224 \frac{r^2}{\tau_{1/2}}, \text{ where r is the radius of the bleached region.}$$

9

Theoretical model for filament sliding: Myosin1b as a catch bond motor

Myosin 1b motor:

Myo1b is identified as a molecular motor with a catch-bond detachment rate: it responds to small resisting loads by dramatically increasing its duty ratio [9]. Single molecule experiments have established that the motor cycle of Myo1b contains two distinctive steps. In sub-step 1, the motor performs a first power stroke of size $d_1 = 5.1$ nm. From sub-step 1, the motor transits to sub-step 2 (Fig. 1B). After the transition, the motor relaxes its stress [9] and it performs a second power stroke of size $d_2 = 3.3$nm. The transition rate between sub-step 1 and 2, $\omega_{1-2}(F)$ depends on the applied force on the motor, F, and shows a catch-bond behavior (Fig. 1B). As found in the single molecule experiments by Laakso et al. this step was force sensitive in the direction of forcing. However, in the motility assays experiments, the force on the motor occurs in both directions, *in the direction of sliding*, during the power stroke, and *opposing the direction of sliding*. We define here the powerstroke as the period of the motor cycle where the strain of the motor is positive and pushes the motor in the gliding direction. In this paper, we assume the force sensitivity is equal on both direction. In other words, the transition rate, $\omega_{1-2}(F)$ is proportional to the absolute value of the force applied on the motor,

$$\omega_{1-2}(F) = \omega_0 \exp\left(-|F|b/(k_B T)\right) + \omega_i. \tag{SE1}$$

Here, ω_i is the force independent transition rate observed at large force, ω_0, the force-dependent transition rate at vanishing force, b, the distance quantifying the strain sensitivity of the motor and $k_B T$ the thermal energy. After the first power-stroke, because of the catch-bond, the motor remains attached to the gliding filament. To prevent unphysical stretching of the motors, they relax their strain and transit to sub-step 2 behind a critical stretching length of the motor $l_{max} = v_f t_{max}$[36], where t_{max} is the maximal attachement time corresponding to a filament sliding at a speed v_f. Behind an extension larger than l_{max}, the motor spring is non linear and the spring strongly stiffens, hence behind this threshold, the transition rate to sub-step 2 becomes infinite. Eventually, after performing a second power-stroke, the motor detaches from the filament with a rate that depends on ATP concentration, C_{ATP}, $\omega_{det}(C_{ATP})$, and follows Michaelis-Menten kinetics,

$$\omega_{det}(C_{ATP}) = \omega_{sat} \frac{C_{ATP}}{C_{ATP} + C^*} \tag{SE2}$$

where ω_{sat} is the detachment rate at saturated ATP concentrations and C^* the characteristic value above which the rate ω_{det} saturates.

Three-state crossbridge model:

To describe the actin filament sliding over Myo1b motors and to include the force and ATP dependences of the motor cycle, we extend the classical cross-bridge model [11,41] by explicitly including the force-and ATP dependent sub-steps of the motor cycle as depicted in Fig.1b. This model is valid for a filament sliding at constant velocity v_f and in the limit of a large number of molecular motors propelling the filament.

An actin filament sliding at speed v_f is transiently attached to a motor in either of the sub-steps 1 or 2, discussed in the previous paragraph (Fig. 1b). We assume here that the two powerstrokes are instantaneous. While the motor is in sub-step 1, it exerts a force on the filament:

$$F_1 = -k_{cb}(v_f \tau_1 - d_1), \tag{SE3}$$

where k_{cb} is the cross-bridge stiffness of the motor and τ_1 is the time since attachment to the filament (the "age" of the motor in sub-step 1) and d_1 the amplitude of the powerstroke. Similarly, while the motor is in sub-step 2, it exerts a force on the filament of magnitude,

$$F_2 = -k_{cb}(v_f \tau_2 - d_2), \tag{SE4}$$

where τ_2 is now the age of the motor in sub-step 2, i.e. the time since the transition to sub-step 2. The fraction of attached motors along the filament, both in sub-step 1, ρ_1, and in sub-step 2, ρ_2, as function of their respective ages, τ_1 and τ_2, evolve according to the following kinetic equations

$$\partial_{\tau_1} \rho_1 = -\omega_{1-2}(F)\rho_1 + \delta(\tau_1)\omega_{on} n_d, \tag{SE5}$$

10

where $\delta(\tau_1)$ is the Dirac delta function, ω_{on} is the attachment rate and n_d is the fraction of detached motors. Note that we assume that during the powerstroke, the motor does not detach, i.e., $\omega_{1-2}(\tau < d_1/v_f) = 0$. We also ignore here, in a mean field approximation, the effect of thermal fluctuations upon attachment of the motors and during the transition between state 1 and state 2. Still, during the transition between states 1 and 2, the thermal fluctuations play an important role in relaxing the strain created on the motro during state 1. Equivalently, ρ_2 evolves as,

$$\partial_{\tau_2}\rho_2 = -\omega_{det}(ATP)\rho_2 + \delta(\tau_2)\int_0^{t_{max}} \rho_1(\tau_1)\omega_{1-2}(F)d\tau_1. \tag{SE6}$$

Solving this set of equations requires the determination of the total fraction of detached motors, n_d, which is obtained by summing the two populations of attached motors,

$$(1 - n_d) = \int_0^{t_{max}} \rho_1(\tau_1)d\tau_1 + \int_0^{t_{max}} \rho_2(\tau_2)d\tau_2. \tag{SE7}$$

The time-averaged force exerted by a single molecular motor along the filament is the sum of the contributions of the motors in sub-steps 1 and 2,

$$F_{mot} = -k_{cb}\left(\int_0^{t_{max}} (v_f\tau_1 - d_1)\rho_1(\tau_1)d\tau_1 + \int_0^{t_{max}} (v_f\tau_2 - d_2)\rho_2(\tau)d\tau_2\right). \tag{SE8}$$

In Fig. S3 A,B we plot the integrands of the two contributions as functions of the motor ages in the corresponding sub-steps for (A) $C_{ATP} = 0.2$ mM and (B) $C_{ATP} = 2$ mM. We use here the kinetic and mechanical parameters given in Table I, (see next section for the choice of these parameters). This figure shows that, initially, when $\tau < d/v_f$ the motor is under positive strain and exerts a positive (propelling) force due to the power stroke, while for $\tau > d/v_f$ the motor is nuder negative strain and exerts an opposing frictional force. Note that is implies that the motor can transit to sub-step 2 *during* the power stroke as well as *after* the power-stroke. Since the time the motor spends performing the power stroke is small $< d_1/v_f \approx 0.25s$, motors rarely transit to sub-step 2 without completing their power-stoke. Moveover, we choose a maximal extension of the motor of $50 - 125$nm, which, at a sliding speed of 25nm/s, correpsonds to a maximal transition time $t_{max} \approx 2 - 5$sec. This value has been based on maximal extensions in single molecule experiments on muscle motor myoII[42]. Morever note that, as can be seen in Fig.S3A, only a tiny fraction $< 10^{-3}$ are still attached at this attachment times.

Depending on the relative values of the kinetic parameters, we identify two regimes. In the limit $\omega_{1-2}(F) \gg \omega_{det}(C_{ATP})$, the ATP dependent detachment is the limiting step and the motor mainly resides in sub-step 2 (Fig. S3C). This typically corresponds to low ATP concentrations. When $\omega_{1-2}(F) \ll \omega_{det}(C_{ATP})$, the motor mainly resides in sub-step 1 and the force dependent (catch-bond) transition between sub-steps 1 and 2 impacts the detachment : this can be seen through the long tail in the force exerted by motors in sub-step 2 in Fig S3B. To emphasize the role of the motor kinetics we show in Fig. S3D that a larger attachment rate ω_{on} increases the fraction of motors attached to the filament and also the fraction of motors in the force dependent sub-step 1, n_1. A larger value of ω_{on} increases the fraction of time that the motor resides in the force dependent sub-step 1 and therefore the impact of the catch-bond on the filament sliding becomes more important.

To further illustrate the role of the catch bond on the motor cycle, we plot the fraction of motors in sub-step 1 ,n_1, and sub-step 2, n_2, and compare a catch-bond motor as described above with a slip-bond motor where the transition rate is force independent $\omega_{1-2} = \omega_i + \omega_0$. We indeed observe that upon increasing the ATP concentration the fraction of motors in sub-step 1 remains constant for the slip-bond motor, in contrast to the catch-bond motor for which n_1 increases. The fraction of motors in sub-step 2 naturally decreases upon increasing C_{ATP}. The increased fraction of motors in sub-step 1 increases the friction between the filament and the motor, decreasing the sliding velocity, relative to the velocity for a slip-bond motor (Fig. S3F).

Determination of the Myo1b transition and detachment rates:

In this section, we estimate the kinetic rates and mechanical parameters of the Myo1b motor at the ATP concentrations used in our experiments. The values reported for the (un)-binding kinetics in Laakso et al. [9] were obtained at significantly lower ATP concentrations ($C_{ATP} = 50\mu M$) than reported here ($C_{ATP} = 0.2 - 2\ mM$). Using these values would imply attachment times up to 10-100 seconds, which are not compatible with sliding speeds of the order of 50nm/s; indeed they would imply stretching the Myo1b motor up to microns. Moreover it is worth noting that

the detachment rates reported in Laakso et al. [9] are the combined kinetic rates of the two sub-steps (sub-step 1 - 2) and (sub-step 2 - detached). Therefore we use the measured sliding velocities at the two ATP concentrations of our experiments to determine ω_i, ω_0 and ω_{sat} (See SE1 and SE2). As already stressed earlier, given the measured speeds we consider that the transition and detachment rates cannot be larger that one second, since otherwise this would imply motor extension larger than 50nm.

To match ω_{sat}, ω_0 and ω_i, we calculate the difference of the predicted and measured sliding speed at $v_f(C_{ATP} = 0.2$ mM$)$: $v_f = 25$nm/s and $v_f(C_{ATP} = 2$ mM$)$: $v_f = 55$nm/s,

$$\text{error} = (v_f(C_{ATP=0.2mM}) - 25\text{nm/s})^2 + (v_f(C_{ATP=2mM}) - 55\text{nm/s})^2. \tag{SE9}$$

By calculating an error map as a function of ω_i and ω_0 for a range of ω_{sat} values we found that $\omega_{sat} \approx 25s^{-1}$ provides optimal matches in sliding speed relative to our experiments (Fig. S4A and S4B). In Fig. S4C and S4E we show the respective values of the error for $\omega_{sat} = 10$ s^{-1} and $\omega_{sat} = 40$ s^{-1} are much higher relative to the $\omega_{sat} \approx 25s^{-1}$ plot (Fig. S4D).

Globally, this analysis provides a band of values that match the sliding velocities at ATP concentrations of 0.2 and $2 \ mM$. This range of values that match the sliding velocities at both ATP concentrations (Indicated in Red in Fig S4D) and corresponds to two regimes: weakly catch bond ($\omega_0/\omega_i \approx 1$) and strong catch-bonds ($\omega_0/\omega_i \gg 1$). The strength of the catch-bond is characterized by the ratio between ω_0 (which is the transition ratio at vanishing force, Eq. SE1) and ω_i (which is the transition rate at high force, Eq. SE1). For our further analysis we choose values as indicated in Table I.

Symbol	Value	Description
ω_i	$1.8s^{-1}$ †	Detachment rate of sub-step 1 at saturated force (SE1)
ω_0	$62s^{-1}$ †	Detachment rate of sub-step 1 at vanishing force (SE1)
ω_{sat}	$25s^{-1}$ †	Detachment rate of sub-step 2 at saturated ATP concentration (SE2)
ω_{on}	$100s^{-1}$ †	Attachment rate of sub-step 1
t_{max}	4 s †	Maximal attachment time of the motor
C^*	1 mM	The characteristic value above which the ω_{det} saturates
b	12 nm ‡	Distance characterizing the strain sensitivity of the motor
k_{cb}	0.2 pN/nm +	Cross-bridge stiffness of the motor

TABLE I: Kinetic parameters. †: Obtained by fitting the measured filament sliding speed v_f, ‡ [9], + : note that this value was determined for Myosin 1c and does not vary widely between different motor species and that the exact numerical value does not change our results qualitatively, e.g. for Myosin II, [41].

Filament sliding enhances actin depolymerization:

We showed in the previous section that due to the catch-bond characteristic of Myo1b, the motor spends a larger time in catch-bond sub-step 1. Here we hypothesise that the prolonged attachment time of the last Myo1b motor to the barbed end of the filament induces a transient stress, and enhances the depolymerization. Experimentally (Fig. 2D), we show that, while the polymerization rate remains unaltered for filaments sliding over Myo1b, the depolymerization rate of the actin filament increases. This effect can be described by the average force dependent depolymerization rate [15],

$$k_{off} = k_{off}^0 \left(n_d + \int_0^{-d_1/v_f} \rho_1(\tau_1)d\tau_1 + \int_0^{-d_2/v_f} \rho_2(\tau_2)d\tau_2 + \int_{-d_1/v_f}^{t_{max}} \rho_1(\tau_1) \exp\frac{k_{cb}(v_f\tau_1 - d_1)}{f^*}d\tau_1 \right.$$
$$\left. + \int_{-d_2/v_f}^{t_{max}} \rho_2(\tau_2) \exp\frac{k_{cb}(v_f\tau_2 - d_2)}{f^*}d\tau_2 \right), \tag{SE10}$$

where k_{off}^0 is the depolymerization rate in the absence of applied force and f^* is the characteristic scale for the force sensitivity of the depolymerization rate. Since in the experiment, the filaments slide over catch-bond motors, the effective opposing frictional force on the filament is increased, enhancing the force at the plus-end and hence the depolymerization. Using SE10 we estimate the predicted increase in depolymerization rate as a function of ATP concentration for various values of the characteristic force, f^* (Fig. S5A). Note also that, depending on f^* this

12

depolymerization rate may diverge in our theoretical model. We find that for $\omega_{on} = 100$ s^{-1}, $3.5 < f^* < 4.5$ pN matches best our experimentally observed depolymerization rates.

The value of the attachment rate ω_{on} (detached - sub-step 1) is a parameter that does not impact the sliding velocity at vanishing external force $F_{mot} = 0$. However, increasing ω_{on}, increases the fraction of motors in sub-step 1 and sub-step 2 as depicted in Fig S3D. Indeed, an increase of ω_{on} leads to a larger number of motor cycles per unit time and therefore to a larger total time that the motor spends in the catch-bond sub-step ρ_1. However, particularly at high ATP concentration, it shifts the equilibrium fraction from a sub-step, primarily dominated by the ATP dependent sub-step 2, to a sub-step dominated by the force dependent catch bond sub-step 1 (Fig. S3E). Choosing a value for ω_{on} in the range of $10 - 10^3$ does not qualitatively impact the results at the experimental ATP concentrations as we show in Fig. S5B.

Identifying that myoII is a weak catch bond motor, we model it with a single force-independent rate ($\omega_0 = \omega_i = 0$), a power-stroke $d = 5.0$ nm and a cross-bridge stiffness $k_{cb} = 0.4$ pN/nm [11]. In Fig. 2b we observe that at $C_{ATP} = 2.0$mM, the sliding velocity is $v_f \approx 255$nm/s. We calculate ω_{sat} that matches this sliding velocity: $\omega_{sat} \approx 82$ s^{-1}. Using this value, we plot the effect of the motors on the depolymerization rate of actin as a function of ω_{on} and find a small enhancement of the depolymerization rate $< 10\%$ for $\omega_{on} = 1 - 10^2$ s^{-1}, in agreement with our experimental data.

Taken together our model shows two interesting features. First, since the filaments are sliding on catch-bond Myo1b motors, their sliding speed decreases while the effective friction exerted by the motors on the filament increases. Second, increasing the sliding velocity by e.g. increasing the ATP concentration increases the time that the motor spend under tension; it increases therefore the total friction force experienced by the filament and hence enhances the depolymerization.

In order to explicitly account for the density of motors along the actin filament, we now derive the sliding velocity of the filament in the gliding assay from the balance between the motor driving force, F_{mot}, and the drag force on the filament due to its surrounding $NF_{mot} = \xi v_f$ (N is the total number of motors along the filament). Depending on the magnitude of the friction coefficient, ξ, a decrease of the number of motors along the filament slows down the filament sliding v_f. This rationalizes the decrease of sliding velocity observed upon lowering the density of motors in the gliding assay (Fig. S2C, Table S1). In addition, a decrease of the motor density along the filament lowers the enhancement of depolymerization since the motors spend less time in the catch-bond sub-step 1 (Fig. S3E), in agreement with our measurements (Table S2).

Filament sliding on a lipid bilayer:

In order to estimate how the motor force is transmitted to the filament when the molecular motors are immersed in a lipid bilayer, instead of being rigidly anchored to a solid surface, we write a simplified force balance between the viscous friction force of the motor/filament and the force exerted by the molecular motors nF_{mot} where $n = \rho\ell$ is the number of attached motors along the filament of length ℓ,

$$-\xi_f \hat{v}_f = nF_{mot} \tag{SE11}$$

$$-\xi_f \hat{v}_f = -n\xi_m v_m \tag{SE12}$$

where ξ_m is the in-plane friction coefficient of the motor complex in the lipid bilayer, v_m, the speed of a molecular motor, ξ_f, the friction coefficient between the filament and the surrounding solution and $\hat{v}_f$, the speed of the filament in the assay. The first equation is the force balance on the filament and the second equation is the force balance on the filament and motors complex. We use here a simplified expression for the motor force estimated in Eq. SE 8, i.e., [41],

$$F_{mot} = f_s \left(1 - \frac{v_m - \hat{v}_f}{v_0}\right), \tag{SE13}$$

where f_s is the stall force of one motor and v_0 the motor speed at vanishing external force ($f_s \approx O(1)$ pN and $v_0 \approx 50$nm/s as calculated before with the more detailed model). The friction between the filament and the solution can be estimated as $\xi_f \approx 2\pi\eta_b/(\log \ell/b_f) \approx O(10^{-8})$ Pa.s.m, where we use the bulk viscosity of water $\eta_b = O(10^{-3})$ Pa.s and as a cut-off lengthscale, the size of the filament $\ell = O(10^{-5})$ m . Note however that the effective bulk viscosity

can be significantly larger since the filament slides close to a surface. The friction between the motor complex and the lipid membrane is $\xi_m \approx 4\pi\eta_m/\log(l_0/L) \approx O(10^{-9})$ Pa.s.m [43], where L is the size of the membrane and l_0 the size of a motor (we estimate the membrane viscosity as $\eta_m \approx O(10^{-10})$ Pa.s. [4] and $\log(L/l_0) \approx O(1)$). Solving equations SE 11 and SE 12 gives the following values for the velocity of the filament, $\hat{v}_f$, relative to the velocity at zero external force on a solid substrate, v_0,

$$\frac{\hat{v}_f}{v_0} = -\frac{n\xi_m}{\xi_f + n\xi_m + v_0\xi_f\xi_m/f_s}, \tag{SE14}$$

and for the velocity of the motor, v_m,

$$\frac{v_m}{v_0} = \frac{\xi_f}{\xi_f + n\xi_m + v_0\xi_f\xi_m/f_s}, \tag{SE15}$$

For realistic values of the friction coefficient of water and typical force values we obtain a filament speed which is very close to the filament speed on a solid substrate $\frac{\hat{v}_f}{v_0} \approx 1$, indicating that, since the in-plane membrane friction of the motor is larger than the filament friction with the fluid, the motors are effectively immobile. However, upon increasing the viscous friction between the filament and the bulk by one/two orders of magnitude, potentially due to inter-filament friction (at high filament density) or to the addition of methylcellulose, the sliding speed of the filament diminishes significantly (Fig. S7). Also decreasing the density of motors along the filament impacts the sliding speed since the effective friction between membrane and motor is proportional to the density of motors.

14

References

1.   Köster DV, Mayor S. Cortical actin and the plasma membrane: inextricably intertwined. *Curr. Opin. Cell Biol.* 2016, **38:** 81-89.

2.   Pyrpassopoulos S, Arpağ G, Feeser EA, Shuman H, Tüzel E, Ostap EM. Force Generation by Membrane-Associated Myosin-I. *Sci. Rep.* 2016, **6:** 25524.

3.   McIntosh BB, Ostap EM. Myosin-I molecular motors at a glance. *J. Cell Sci.* 2016, **129:** 2689-2695.

4.   Almeida CG, Yamada A, Tenza D, Louvard D, Raposo G, Coudrier E. Myosin 1b promotes the formation of post-Golgi carriers by regulating actin assembly and membrane remodelling at the trans-Golgi network. *Nat. Cell Biol.* 2011, **13:** 779-789.

5.   Gupta P, Gauthier NC, Cheng-Han Y, Zuanning Y, Pontes B, Ohmstede M*, et al.* Myosin 1E localizes to actin polymerization sites in lamellipodia, affecting actin dynamics and adhesion formation. *Biol. Open* 2013, **2:** 1288-1299.

6.   Iuliano O, Yoshimura A, Prospéri M-T, Martin R, Knölker H-J, Coudrier E. Myosin 1b promotes axon formation by regulating actin wave propagation and growth cone dynamics. *J. Cell Biol.* 2018, **217:** 2033.

7.   Joensuu M, Belevich I, Rämö O, Nevzorov I, Vihinen H, Puhka M*, et al.* ER sheet persistence is coupled to myosin 1c–regulated dynamic actin filament arrays. *Mol. Biol. Cell* 2014, **25:** 1111-1126.

8.   Greenberg MJ, Lin T, Goldman YE, Shuman H, Ostap EM. Myosin IC generates power over a range of loads via a new tension-sensing mechanism. *Proc. Natl Acad. Sci. USA* 2012, **109:** E2433-E2440.

9.   Laakso JM, Lewis JH, Shuman H, Ostap EM. Myosin I can act as a molecular force sensor. *Science* 2008, **321:** 133-136.

10.   Lewis JH, Lin T, Hokanson DE, Ostap EM. Temperature dependence of nucleotide association and kinetic characterization of Myo1b. *Biochemistry* 2006, **45:** 11589-11597.

11.   Guérin T, Prost J, Joanny J-F. Dynamical behavior of molecular motor assemblies in the rigid and crossbridge models. *The European Physical Journal E* 2011, **34:** 60.

12.   Carlier M-F, Pernier J, Montaville P, Shekhar S, Kühn S. Control of polarized assembly of actin filaments in cell motility. *Cell. Mol. Life Sci.* 2015, **72:** 3051-3067.

13.   Veigel C, Molloy JE, Schmitz S, Kendrick-Jones J. Load-dependent kinetics of force production by smooth muscle myosin measured with optical tweezers. *Nat. Cell Biol.* 2003, **5:** 980.

14.   Crevenna AH, Arciniega M, Dupont A, Mizuno N, Kowalska K, Lange OF*, et al.* Side-binding proteins modulate actin filament dynamics. *eLife* 2015, **4:** e04599.

15

15. Footer MJ, Kerssemakers JWJ, Theriot JA, Dogterom M. Direct measurement of force generation by actin filament polymerization using an optical trap. *Proc. Natl Acad. Sci. USA* 2007, **104:** 2181-2186.

16. Komaba S, Coluccio LM. Localization of Myosin 1b to Actin Protrusions Requires Phosphoinositide Binding. *J. Biol. Chem.* 2010, **285:** 27686-27693.

17. Guo L, Har JY, Sankaran J, Hong Y, Kannan B, Wohland T. Molecular diffusion measurement in lipid bilayers over wide concentration ranges: a comparative study. *ChemPhysChem* 2008, **9:** 721-728.

18. Pyrpassopoulos S, Feeser EA, Mazerik J, Tyska M, Ostap M. Membrane-bound Myo1c powers asymmetric motility of actin filaments. *Curr. Biol.* 2012, **22:** 1688-1692.

19. Grover R, Fischer J, Schwarz FW, Walter WJ, Schwille P, Diez S. Transport efficiency of membrane-anchored kinesin-1 motors depends on motor density and diffusivity. *Proc. Natl Acad. Sci. USA* 2016, **113:** E7185.

20. Vogel SK, Petrasek Z, Heinemann F, Schwille P. Myosin motors fragment and compact membrane-bound actin filaments. *eLife* 2013, **2:** e00116.

21. Murrell M, Gardel ML. F-actin buckling coordinates contractility and severing in a biomimetic actomyosin cortex *Proc. Natl Acad. Sci. USA* 2012, **109:** 20820-20825

22. Kovar DR, Kuhn JR, Tichy AL, Pollard TD. The fission yeast cytokinesis formin Cdc12p is a barbed end actin filament capping protein gated by profilin. *J. Cell Biol.* 2003, **161:** 875.

23. Romero S, Le Clainche C, Didry D, Egile C, Pantaloni D, Carlier M-F. Formin Is a Processive Motor that Requires Profilin to Accelerate Actin Assembly and Associated ATP Hydrolysis. *Cell* 2004, **119:** 419-429.

24. Johnston AB, Collins A, Goode BL. High-speed depolymerization at actin filament ends jointly catalysed by Twinfilin and Srv2/CAP. *Nat. Cell Biol.* 2015, **17:** 1504.

25. Wioland H, Guichard B, Senju Y, Myram S, Lappalainen P, Jégou A, *et al.* ADF/Cofilin accelerates actin dynamics by severing filaments and promoting their depolymerization at both ends. *Curr. Biol.* 2017, **27:** 1956-1967.e1957.

26. Varga V, Leduc C, Bormuth V, Diez S, Howard J. Kinesin-8 Motors Act Cooperatively to Mediate Length-Dependent Microtubule Depolymerization. *Cell* 2009, **138:** 1174-1183.

27. Moores CA, Milligan RA. Lucky 13-microtubule depolymerisation by kinesin-13 motors. *J. Cell Sci.* 2006, **119:** 3905-3913.

28. Greenberg Michael J, Arpağ G, Tüzel E, Ostap EM. A perspective on the role of Myosins as mechanosensors. *Biophys. J.* 2016, **110:** 2568-2576.

29.   Dürre K, Keber FC, Bleicher P, Brauns F, Cyron CJ, Faix J, *et al.* Capping protein-controlled actin polymerization shapes lipid membranes. *Nat. Commun.* 2018, **9:** 1630.

30.   Ennomani H, Letort G, Guérin C, Martiel J-L, Cao W, Nédélec F, *et al.* Architecture and Connectivity Govern Actin Network Contractility. *Curr. Biol.* 2016, **26:** 616-626.

31.   Freeman SA, Jaumouillé V, Choi K, Hsu BE, Wong HS, Abraham L, *et al.* Toll-like receptor ligands sensitize B-cell receptor signalling by reducing actin-dependent spatial confinement of the receptor. *Nat. Commun.* 2015, **6:** 6168.

32.   Noguchi T, Lenartowska M, Miller KG. Myosin VI stabilizes an actin network during Drosophila spermatid individualization. *Mol. Biol. Cell* 2006, **17:** 2559-2571.

33.   Loubéry S, Delevoye C, Louvard D, Raposo G, Coudrier E. Myosin VI Regulates Actin Dynamics and Melanosome Biogenesis. *Traffic* 2012, **13:** 665-680.

34.   Ciobanasu C, Faivre B, Le Clainche C. Actomyosin-dependent formation of the mechanosensitive talin–vinculin complex reinforces actin anchoring. *Nat. Commun.* 2014, **5:** 3095.

35.   Pollard TD. Myosin Purification and Characterization. In: *Methods in Cell Biology*, vol. 24. Elsevier Inc., 1982, pp 333-371.

36.   Yamada A, Mamane A, Lee-Tin-Wah J, Di Cicco A, Prévost C, Lévy D, *et al.* Catch-bond behaviour facilitates membrane tubulation by non-processive myosin 1b. *Nat. Commun.* 2014, **5:** 3624.

37.   Weinberger A, Tsai F-C, Koenderink G, Schmidt T, Itri R, Meier W, *et al.* Gel-assisted formation of Giant Unilamellar Vesicles. *Biophys. J.* 2013, **105:** 154-164.

38.   Galush WJ, Nye JA, Groves JT. Quantitative fluorescence microscopy using supported lipid bilayer standards. *Biophys. J.* 2008, **95:** 2512-2519.

39.   Sorre B, Callan-Jones A, Manzi J, Goud B, Prost J, Bassereau P, *et al.* Nature of curvature-coupling of amphiphysin with membranes depends on its bound density. *Proc. Natl Acad. Sci. USA* 2012, **109:** 173-178.

40.   Soumpasis DM. Theoretical analysis of fluorescence photobleaching recovery experiments. *Biophys. J.* 1983, **41:** 95-97.

41.   Vilfan A, Frey E, Schwabl F. Force-velocity relations of a two-state crossbridge model for molecular motors. *Europhys. Lett.* 1999, **45**: 283-289.

42.   Schwaiger I, Sattler C, Hostetter DR, Rief M. The myosin coiled-coil is a truly elastic protein structure. *Nat. Mater*. 2002, **1**: 232-235.

43.   Saffman PG, Delbrück M. Brownian motion in biological membranes. *Proc. Natl. Acad. Sci. USA* 1975, **72**: 3111-3113.

Acknowledgments

Author contributions

P.B and E.C. designed the study. J.P. and A.M. performed TIRF experiments and analyzed data; J.P. and T.L. conducted FRAP experiments; H.B. purified Myosin 1b. R.K. and J.-F.J. developed the model. P.B, E.C., J.P., R.K. and J.-F.J. wrote the paper.

Competing interests

The authors declare no competing interests.

Figure Legends

Figure 1: **Three-state cross-bridge model and Myo1b-Actin gliding assays**. **(A)** Schematic representation of domain organization of Myo1b. Motor domain (blue); Light Chain Binding Domain (LCBD) (yellow); TH1 domain (red), PH domain (cyan) that binds phosphoinositides. **(B)** Three-state cross-bridge model. The motor binds to the filament with an attachment rate ω_{on}, then performs a first power-stroke of size d_1=5.1 nm. After this first power stroke the motor transits with a force-dependent (catch-bond) rate ω_{1-2} to release its stress and performs a second power-stroke d_2=3.3 nm. After this second sub-step, the motor binds an ATP molecule and detaches from the filament with a rate ω_{det}. **(C)** Gliding assays of stabilized actin filaments (I-II) and polymerizing actin filaments (III-IV) sliding on Myo1b anchored on coverslip (I-III) or bound to a supported lipid bilayer (II-IV).

Figure 2: **Sliding on immobilized Myosin 1b increases F-actin depolymerization.** **(A)** Representative kymographs of stabilized F-actin (top) or polymerizing F-actin with 0.6 µM G-actin (bottom), on uncoated glass or sliding on glass coated with Myo1b (2 mM and 0.2 mM ATP (see movies S2 and S3) or MyoII (see movie S6). The sliding distance $\varDelta X$ and the elongation $\varDelta L$ of the filaments are indicated by white arrows. Actin fluorescence intensity is represented according to the "Fire" LUT of Image J. Scale bar, 5µm. 1 image/10 sec. **(B)** Dot plot representation of the sliding velocities v_f of stabilized (top) and polymerizing actin filaments (0.6 µM G-actin) (bottom) on immobilized Myo1b (8000 molecules/µm^2) at 2 mM (blue) or 0.2 mM (grey) ATP or sliding on MyoII at 2 mM ATP (orange). The number of analyzed filaments and the mean-values ± s.e.m. are indicated. **(C)** Filament elongation ΔL (normalized by the length of the actin subunit (su) equal to 2.7 nm) versus time for filaments shown in A (bottom) in the absence of myosins and in the presence of MyoII or Myo1b at two ATP concentrations. The polymerization rate at the barbed end v_p (in su/s) is deduced from the slope. **(D)** v_p as a function of G-actin concentration C_m for the different conditions. The fits correspond to $v_p = k_{on}C_m - k_{off}$, with k_{on} the rate of association of G-actin and k_{off} the rate of dissociation. C_{c+} is the critical concentration for polymerization. Inset: k_{off} for the different conditions. Error bars represent s.e.m. (n>25). **(E)** Model for the role of Myo1b motor on the dissociation (depolymerization) rate k_{off}. The filament, sliding at velocity v_f, experiences a force F_{mot} at the barbed end while the motor is attached, thus impacting k_{off}, but not the association (polymerization) rate k_{on}.

Figure 3: **Sliding on Myosin 1b bound to a supported lipid bilayer increases F-actin depolymerization** **(A)** Top: Diffusion coefficients of Atto488DOPE (DOPE*) and Alexa488-labelled Myo1b (Myo1b*) in a SLB with bound Myo1b, with or without 0.3 % methylcellulose (MEC), and in absence or in the presence of a dense F-actin network (n = 30). See Fig. S6 for representative FRAP experiments. Bottom: Effective diffusion coefficients of Cherry-CAAX, Cherry-Myo1b, expressed in HEK293T cells (n > 5). Error bars represent s.e.m. **(B)** Representative kymographs of non-polymerizing (top) and polymerizing F-actin (bottom) in the presence of 0.6 µM G-actin with Myo1b bound to SLBs (movie S8). Scale bar, 5µm. 1 image/10 sec. **(C)** Dot blot representation of the velocities v_f of stabilized (top) and polymerizing F-actin (bottom) sliding on immobilized Myo1b (dark blue) or on Myo1b bound to a SLB (cyan). The number of analyzed filaments is indicated. **D)** Model for filament sliding: The effective filament sliding is determined by a balance between the viscous dissipation of the motor moving with a velocity v_m in the lipid bilayer with a viscosity η_m and a filament sliding at a velocity v_f in a solution of viscosity η_b. **(E)** ΔL versus time for the single filaments shown in (B). **(F)** v_p as a function of G-actin concentration C_m for the
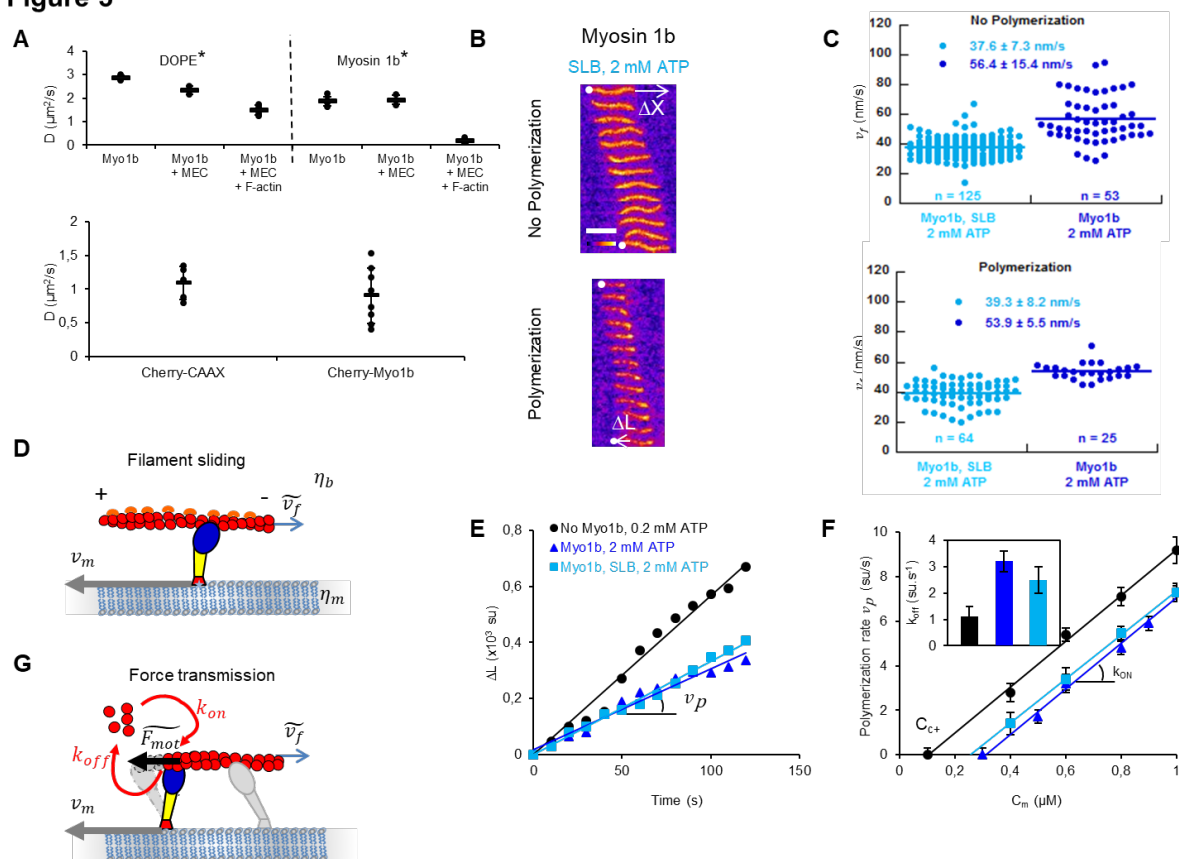
19

different conditions. The fit to the data is the same as in Fig. 2D. Inset: k_{off} for the different conditions. Error bars represent s.e.m. (n>25). **(G)** Model for force transmission: The effective force experienced by the polymerizing filament F_{mot} is diminished by the motion in the lipid bilayer of the motor v_m at the barbed end.

Figure 1
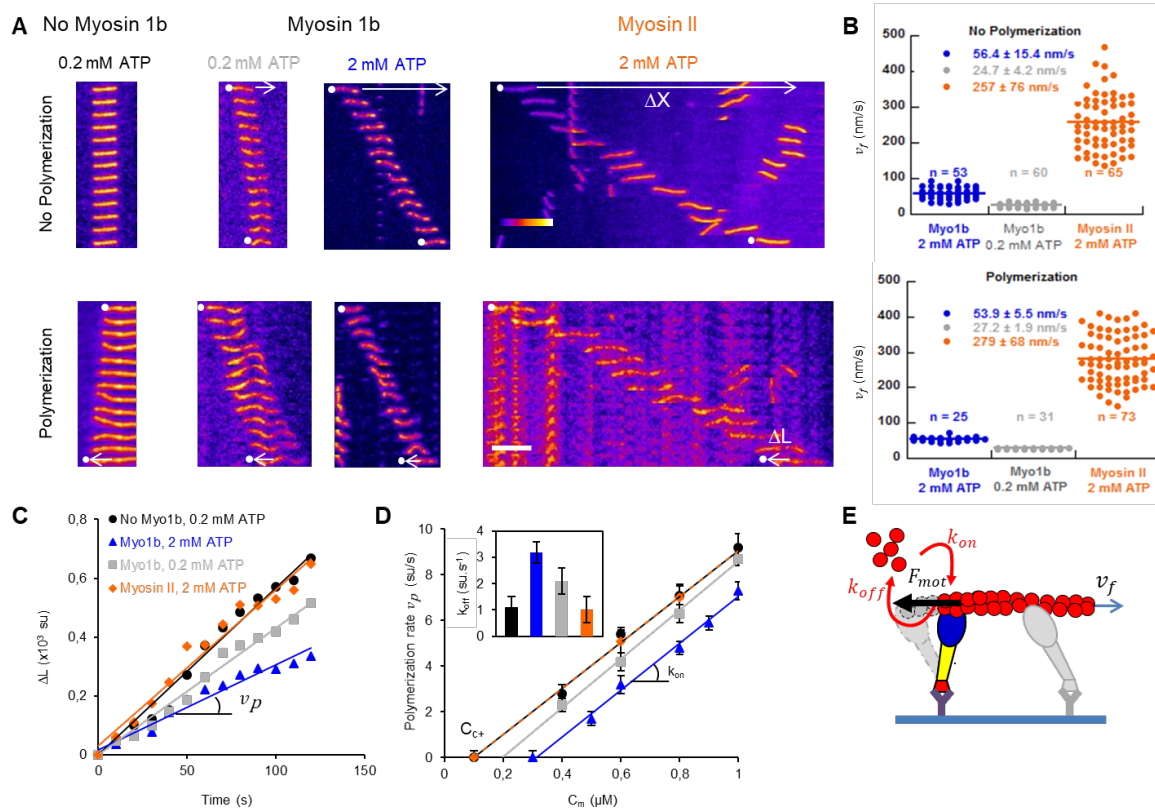
Figure 2

Figure 3

Supplementary information

Legends - Supplementary tables and figures

Table S1: Sliding velocities v_f of stabilized and polymerizing actin filaments on Myo1b or Myosin II in the different used conditions.

Table S2: Rate constants of G-actin monomer association and dissociation in the absence and presence of Myo1b or Myosin II in the different used conditions.

Figure S1: Analysis of the experimental data and calibration of the Myo1b density. **(A)** Left: Time-lapse images obtained by TIRF microscopy of a stabilized filament (top) (and a polymerizing filament in the presence of 1.2 μM G-actin (bottom) sliding along glass-anchored Myo1b (see movie S1). White dots indicate the filament's barbed end. The white dashed represents the trajectory of the stabilized filament, and ΔX the total displacement of the filament over the period considered. L_0 and ΔL are the initial length of the polymerizing filament and its elongation, respectively, both normalized by the actin sub-unit length. Middle: corresponding kymographs. The sliding ΔX and the elongation ΔL correspond to the white arrows. Right: Time variation of ΔX and ΔL. The sliding velocity v_f and the elongation rate v_p are deduced from the slopes of the graphs. Actin fluorescence intensity is represented according to the "Fire" LUT of Image J. Scale bar, 5μm. 1 image/20 sec. **(B)** Myo1b density on the solid substrate or on the supported bilayer deduced from (a) the measurement of the fluorescence intensity of a reference lipid Atto488DOPE at known density in a SLB (supported lipid bilayer), and the comparison of (b) the fluorescence of Myo1b dye Alexa 488 and (c) Atto488DOPE in bulk at known concentrations (see Materials and Methods). The calibration constant A is deduced from the slope of a).

Figure S2: Impact of Myo1b on F-actin pointed end and impact of Myo1b at low density, inactivated, or in solution on the sliding and actin depolymerization at the barbed end. **(A)** Representative kymograph of polymerizing actin filaments, in presence of 0.6 μM G-actin, 2 mM ATP with anchored Myo1b at $\approx$ 8000 μm^{-2} (see movie S4). The elongation ΔL_m of the filaments at the pointed end (between the 2 dashed white lines) is indicated. Scale bar, 5 μm. 1 image/10 sec. **(B)** Representative kymographs of phalloidin stabilized filaments (top) or polymerizing actin filaments (bottom), in presence of 0.6 μM G-actin, 2 mM ATP, with Myo1b in solution (red), Myo1b without motor activity (brown), with anchored Myo1b at low density ($\approx$500 motor/μm^2) (purple). (See movies S2, S3 and S5). Scale bar, 5μm. 1image/10 sec. **(C)** Comparison of the distribution of the velocities v_f of stabilized (top) and polymerizing F-actin (bottom) sliding on immobilized high density Myo1b, 2 mM ATP (dark blue) and 0.2 mM ATP (grey) and low density Myo1b, 2 mM ATP (purple). Velocity distributions and average velocities are indicated. Data are represented with a "Dot plot". The number of analyzed filaments is indicated. **(D)** ΔL versus time for the single filaments for the conditions shown in (A) and (B) and in the absence of Myo1b. **(E)** v_p as a function of G-actin concentration C_m for the different indicated conditions. The fit to the data is the same as in Fig. 2D. Error bars represent s.e.m. (n > 25). Inset: k_{off} for the different conditions. **(F)** Representative kymographs of depolymerizing actin filaments, in absence of G-actin (C_m=

0 μM), without Myo1b (left) or with anchored Myo1b at ≈8000 motor/μm^2 (right), with 2 mM ATP. (See movie S7). Scale bar, 5μm. 1 image/10 sec. **(G)** ΔL versus time for the single filaments shown in (F). **(H)** v_p as a function of filament length L for single polymerizing filaments sliding along glass-anchored Myo1b in the presence of 0.6 μM G-actin and 2 mM ATP (n = 90, v_p measured during 30 sec).

Figure S3: Predictions of our model for filament sliding. (A, B) Forces exerted on the filament $F_1\rho_1$, $F_2\rho_2$ as a function for their respective age of attachment τ_1, τ_2; for (A) C_{ATP} =0.2mM and (B) C_{ATP} = 2mM. **(C, D)** Fractions of motors in sub-state 1 (n_1) and sub-state 2 (n_2) as a function of (C) C_{ATP}, for ω_{on}=100 s^{-1} and (D) ω_{on}, for C_{ATP}=2mM. **(E)** n_1 and n_2 as a function of C_{ATP} for ω_{on}=100 s^{-1}. The dashed line corresponds to a non-catch bond version of the motor with otherwise identical parameters ($\omega_{1-2}= \omega_i+\omega_0$). **(F)** Sliding velocities of the filament v_f as a function of C_{ATP}, corresponding to the curves in (E). In all figures, we have used kinetic and mechanic parameters as described in Table I (Materials and Methods).

Figure S4: Determination of the Myo1b transition rates ($\omega_i, \omega_0, \omega_{sat}$. (A)-(B) Calculated sliding speeds at respectively (A) C_{ATP}=2 mM and (B) C_{ATP} =0.2 mM, as a function of ω_i, ω_0 (SE9). **(C)-(D-(E)** Error map, i.e., the sum of the square difference between the calculated and measured sliding speeds, for three different values of ω_{sat}=10, 25 and 40 s^{-1}. Small matching errors indicate that the sliding speeds match the measured values. Note that the red region in (D) represents the region with small squared error (error < 100(nm/s)^2, see (SE9)), which is never obtained for ω_{sat}=10 and 40 s^{-1}.

Figure S5: Theoretical prediction for the impact of filament sliding on depolymerization. (A) Depolymerization rate relative to that at vanishing external force k_{off}/k_{off}^0 as function of C_{ATP} for various values of the characteristic scale for the force sensitivity of the depolymerization rate of the actin f^*. **(B)** k_{off}/k_{off}^0 as function of ω_{on} at f^*=4 pN for the Myo1b and MyoII motor at C_{ATP}=2mM. See parameter values in Table I (Materials and Methods).

Figure S6: FRAP data of DOPE and Myo1b in a SLB. (A and B) Representative FRAP recovery curves (symbols) and the best fit with single exponential (solid line) of Atto488-DOPE (DOPE*) and Alexa488-labelled Myo1b (Myosin 1b*) in a SLB with bound Myo1b, with (in red) or without (in black) 0.3 % methylcellulose (MEC), and in absence or presence (in cyan) of a dense F-actin network.

Figure S7: Effect of bulk viscosity on relative velocity of the filament. Velocity of the filament v_f, relative to its velocity on a solid substrate v_0 (Eq. SE14), for different values of motor density n. Increasing the bulk viscosity, relative to the membrane viscosity, induces motion of the motors in the bilayer, hence decreasing the effective velocity of the filament. Increasing the density of molecular motors on the surface increases the effective membrane friction and hence increases the sliding speed.

Figure S8: Myo1b bound to giant liposomes produces membrane invagination in presence of stabilized actin filaments. Representative confocal microscopy images of tubules induced by Myo1b bound to a PI(4,5)P$_2$-containing GUV in the presence of stabilized actin filaments. We have observed tubulation in the equatorial plane for 16 GUVs over a total of 96. Labeling corresponds to **(A)** 0.3% Texas Red DHPE (mol/mol) and **(B)** stabilized actin filaments with Alexa Fluor 647 phalloidin. Scale bars, 5 μm.

Legends - Movies

Movie S1: Stabilized and polymerizing actin filaments sliding along glass-anchored Myo1b (corresponding to Fig. S1A).
Sliding of stabilized filaments labeled with phalloidin-Alexa547 (a) and polymerizing filaments (b) with 1.2 μM actin in bulk (10 % Alexa594 labeled), along Myo1b (8000 μm^{-2}) at 2 mM ATP. White arrow indicates the initial position of the filament corresponding to the kymograph in Fig. S1A. Note that no filament breaking is observed during these experiments. Scale bar 5 μm. Time in s.

Movie S2: Effect of the ATP concentration and Myo1b density on stabilized actin filaments sliding along glass-anchored Myo1b (corresponding to Figs. 2A and S2B).
Filaments stabilized with phalloidin-Alexa547 as a function of ATP concentration (0.2 and 2 mM ATP), without Myo1b (a), sliding on Myo1b at high density (8000 μm^{-2}) (b, c) or at low density (400 μm^{-2}) (d). Wide field movies followed by single filament movies corresponding to kymographs shown in Fig. 2A-Top panel and Fig. S2B-Top panel. White arrows indicate the initial position of single filaments. Scale bar 5 μm. Time in s.

Movie S3: Effect of ATP concentration and Myo1b density on polymerizing actin filaments sliding along glass-anchored Myo1b (corresponding to Fig. S2A).
Polymerizing filaments as a function of ATP concentration as a function of ATP concentration (0.2 and 2 mM ATP), without Myo1b (a), sliding on Myo1b at high density (8000 μm^{-2}) (b, c) or at low density (400 μm^{-2}) (d). Wide field movies followed by single filament movies corresponding to kymographs shown in Fig. 2A-Bottom panel and Fig. S2B-Bottom panel. White arrows indicate the initial position of single filaments. Scale bar 5 μm. Time in s.

Movie S4: No effect at pointed-end on polymerizing actin filaments sliding along glass-anchored Myo1b.
Polymerizing actin filaments with 0.6 μM actin (10 % Alexa594 labeled), along Myo1b (8000 μm^{-2}) at 2 mM ATP. The white arrow indicates the initial position of the filament shown in Fig. S2A. Scale bar 5 μm. Time in s.

Movie S5: Stabilized and polymerizing actin filaments with Myo1b in bulk or inactivated (corresponding to Fig. S2B).
Filaments stabilized with phalloidin-Alexa547 and polymerizing actin filament, with 0.6 μM actin (10 % Alexa594 labeled), 2 mM ATP, 300 nM Myo1b in the bulk, or bound but inactivated. Note that in the bottom left movie, one filament seems to move but it suddenly appears in the field of view while sedimenting. Frames correspond to the kymographs shown in Fig. S2B; arrows indicate the initial position of these filaments. Scale bar 5 μm. Time in s.

Movie S6: Stabilized and polymerizing actin filaments sliding along glass-anchored MyoII (corresponding to Fig. 2A).

Filaments stabilized with phalloidin-Alexa547 or polymerizing at 0.6 µM actin (10 % Alexa594 labeled), sliding along MyoII at 2 mM ATP. Frames correspond to the kymographs shown in Fig. 2A; arrows indicate the initial position of these filaments. Scale bar 5 µm. Time in s.

Movie S7: Impact of Myo1b on the depolymerization of actin filaments in the absence of G-actin in the bulk (corresponding to Fig. S2F).
Filaments depolymerizing in the absence of G-actin in bulk, without Myo1b, or sliding along Myo1b, at 2 mM ATP. Frames correspond to the kymographs shown in Fig. S2F; arrows indicate the initial position of these filaments. Scale bar 5 µm. Time in s.

Movie S8: Stabilized and polymerizing actin filaments sliding along Myo1b bound to SLBs (corresponding to Fig. 3B).
Sliding of filaments stabilized with phalloidin-Alexa547 or polymerizing at 0.6 µM actin (10 % Alexa594 labeled), along Myo1b bound to SLBs (≈ 8500 µm^{-2}) at 2 mM ATP. Wide field movies followed by single filament movies corresponding to kymographs shown in Fig. 3B. White arrows indicate the initial position of single filaments. Scale bar 5 µm. Time in s.

27

Table S1

|	Myosin	[ATP] (mM)	Density (molecules/μm^2)	Condition	Velocity (nm/s)
	Myosin 1b	2	8393 ± 430	No polymerization	56.4 ± 15.4
		2	8444 ± 873	Polymerization	53.9 ± 5.5
On glass		0.2	8776 ± 1293	No polymerization	24.7 ± 4.2
		0.2	8876 ± 459	Polymerization	27.2 ± 1.9
		2	447 ± 20	No polymerization	33.3 ± 3.1
		2	533 ± 84	Polymerization	35.6 ± 6.2
	Myosin II	2	Not reported	No polymerization	257 ± 76
		2	Not reported	Polymerization	279 ± 68
On SLB	Myosin 1b	2	8770 ± 170	No polymerization	37.6 ± 7.3
		2	8657 ± 1251	Polymerization	39.3 ± 8.2

Table S2

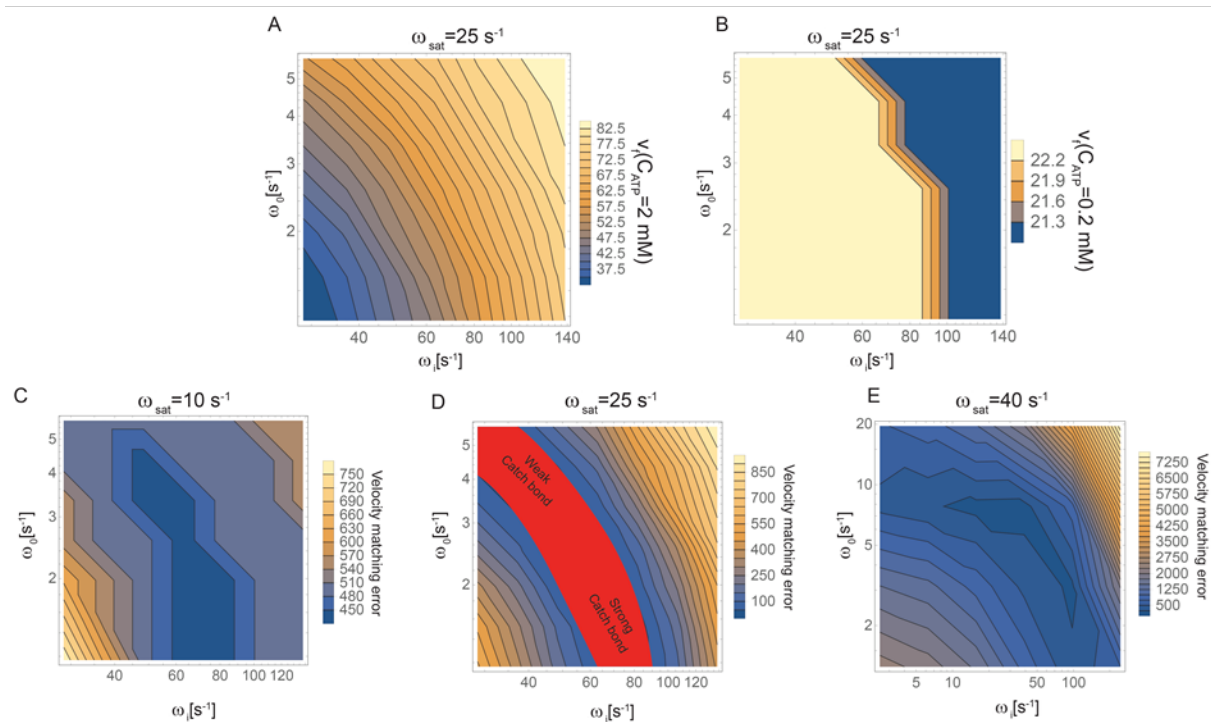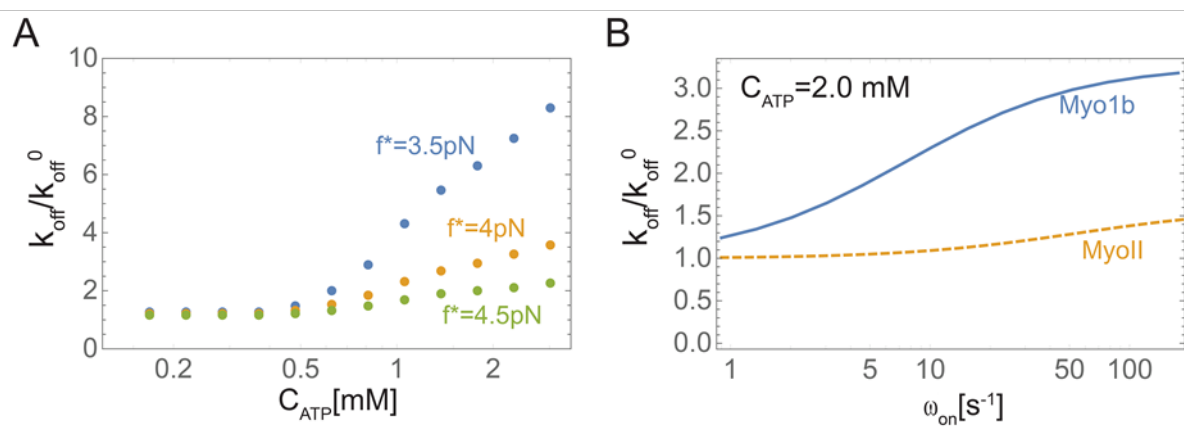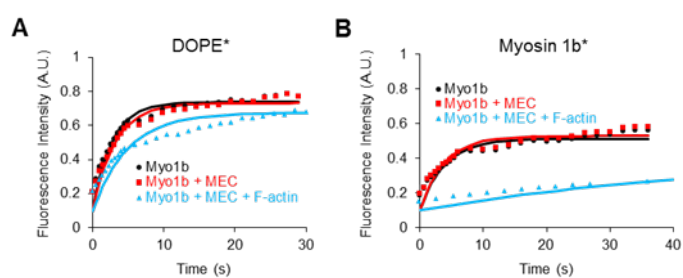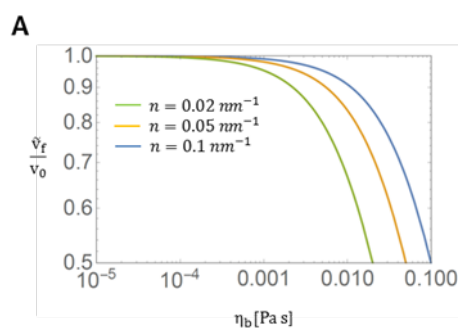|	Myosin	[ATP] (mM)	Density (molecules/μm^2)	k_{on} (su.μM^{-1}.s^{-1})	k_{off} (su.s^{-1})	Critical concentration C_{c+} (μM)
	No Myosin	0.2		10.3 ± 0.8	1.1 ± 0.4	0.10 ± 0.05
	No Myosin	2		10.9 ± 0.6	1.4 ± 0.4	0.13 ± 0.06
In solution	Myosin 1b	2	Not reported	11.4 ± 1.1	1.8 ± 0.5	0.16 ± 0.04
	Myosin 1b	2	8444 ± 873	10.3 ± 0.5	3.2 ± 0.4	0.31 ± 0.05
		0.2	8876 ± 459	10.7 ± 0.9	2.1 ± 0.5	0.20 ± 0.04
On glass		2	533 ± 84	10.0 ± 1.2	2.6 ± 0.6	0.26 ± 0.08
	No motor	2	7767 ± 423	10.9 ± 0.8	1.6 ± 0.5	0.15 ± 0.05
	Myosin II	2	Not reported	10.0 ± 0.8	1.0 ± 0.5	0.10 ± 0.05
On SLB	Myosin 1b	2	8657 ± 1251	9.9 ± 0.8	2.5 ± 0.5	0.26 ± 0.05

Figure S1
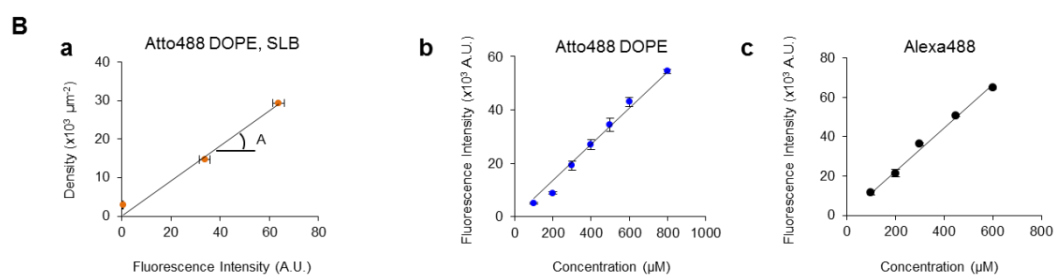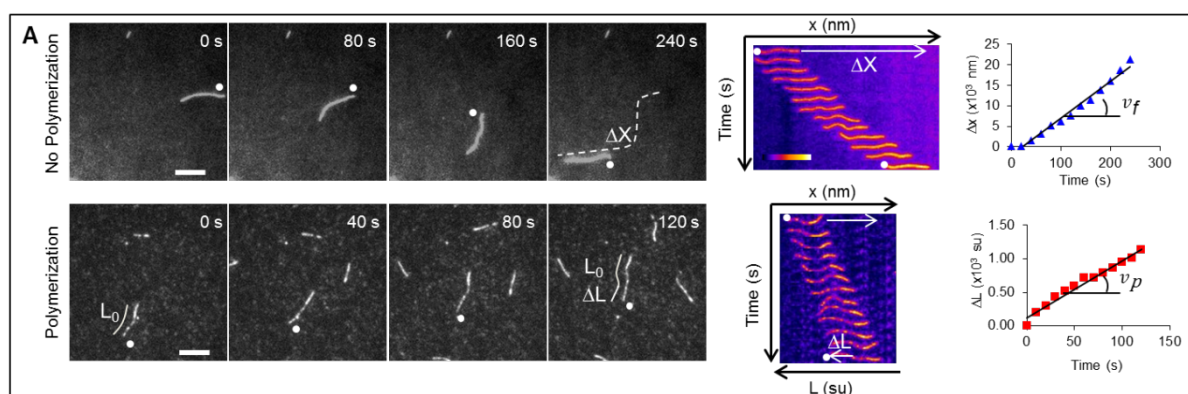
Figure S2
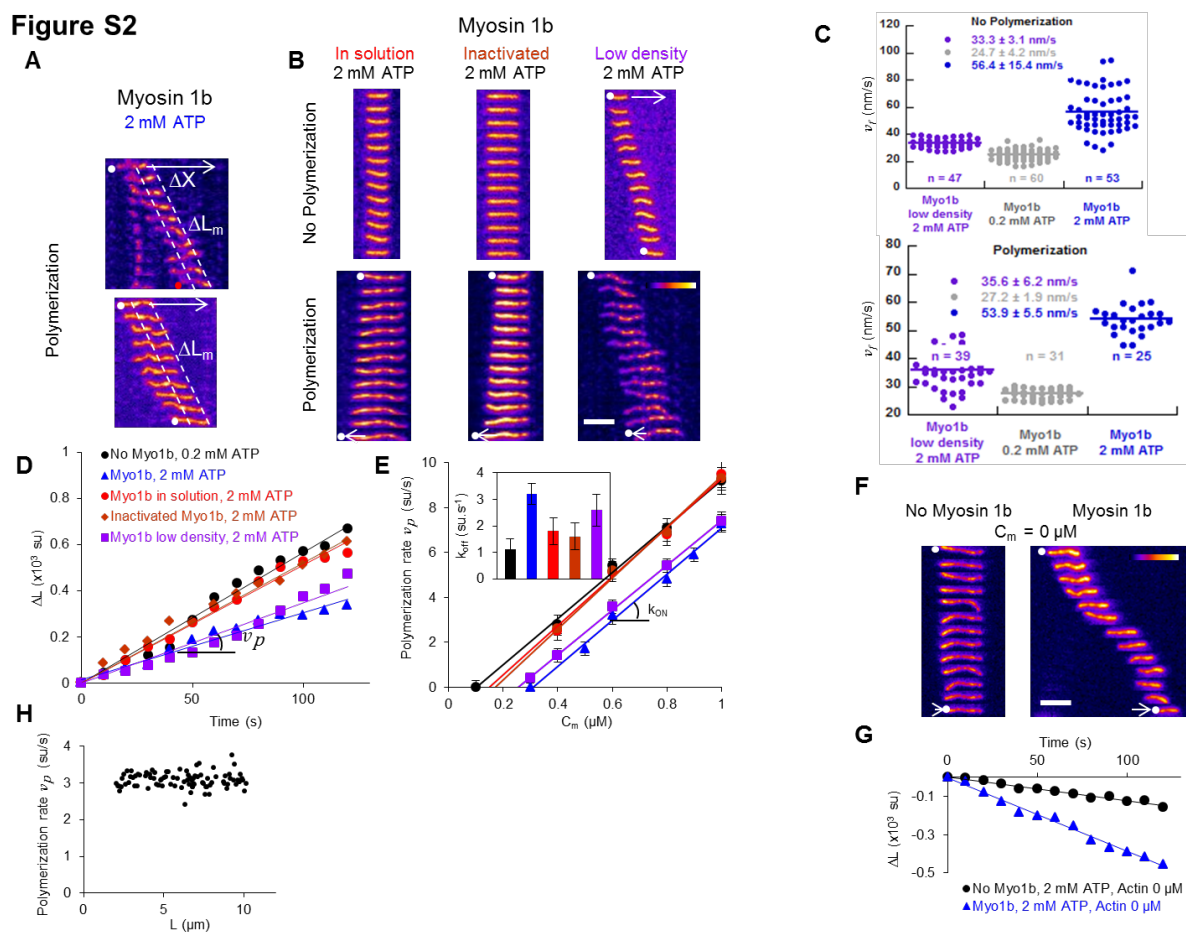
Figure S3
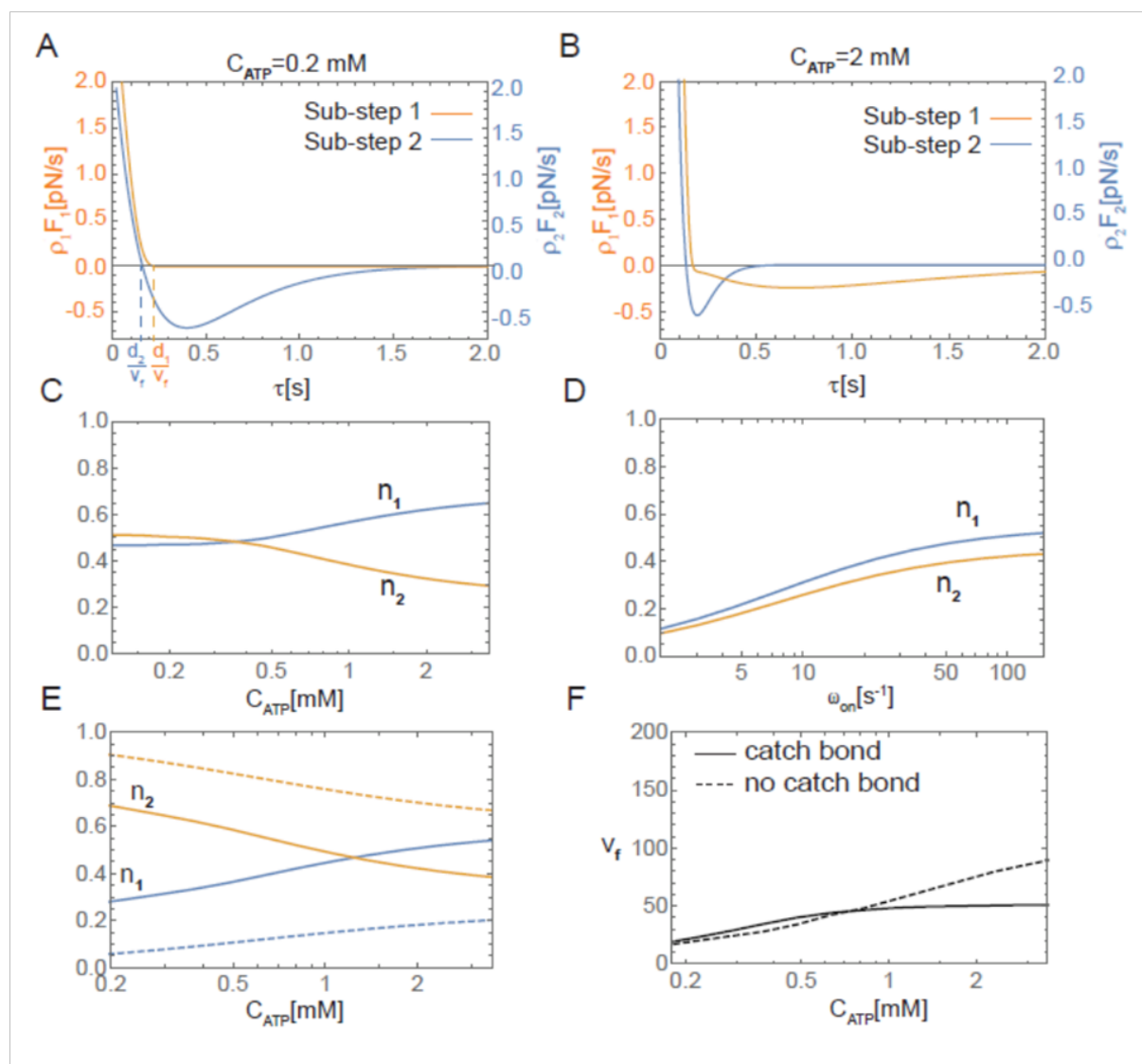
Figure S4

Figure S5

Figure S6

Figure S7

A

Figure S8

A Membrane   **B** F-actin